



Slip band–grain boundary interactions in commercial-purity titanium

Y. Guo^{a,*}, T.B. Britton^b, A.J. Wilkinson^a

^a Department of Materials, University of Oxford, Parks Road, Oxford OX1 3PH, UK

^b Department of Materials, Royal School of Mines, Imperial College London, London SW7 2AZ, UK

Received 4 April 2014; received in revised form 6 May 2014; accepted 6 May 2014

Abstract

The interaction between slip bands and grain boundaries in commercial-purity titanium was examined using cross-correlation-based electron backscatter diffraction. At a low strain level, three types of interactions were observed: blocked slip band with stress concentration; slip transfer; and blocked slip band with no stress concentration. The stress concentration induced by the blocked slip band was fitted with Eshelby's theoretical model, from which a Hall–Petch coefficient was deduced. It was found that the Hall–Petch coefficient varies with the individual grain boundary. We investigated the geometric alignment between the slip band and various slip systems to the neighbouring grain. Stress concentration can be induced by the blocked slip band if the slip system is poorly aligned with $\langle a \rangle$ prismatic, pyramidal or basal slip systems in the neighbouring grain. Transfer of slip across the boundary occurs when there is good alignment on $\langle a \rangle$ prismatic or $\langle a \rangle$ pyramidal slip systems. Other stress-relieving mechanisms are possible when the best alignment is not with the slip system that has the lower critical resolved shear stress.

© 2014 Acta Materialia Inc. Published by Elsevier Ltd. All rights reserved.

Keywords: HR-EBSD; Slip transfer; Slip band; Hall–Petch coefficient; Titanium

1. Introduction

Grain boundaries are effective barriers to dislocation motion, providing a substantial strengthening mechanism for polycrystalline materials [1]. The pile-up of dislocations against grain boundaries could lead to localised high-intensity stress concentrations, especially in planar slip materials. The forward stress generated by the slip band–grain boundary interaction has been cited to lead to slip transfer [2], deformation twin nucleation [3,4], cavity nucleation [5], fatigue crack nucleation [6] and a number of other phenomena [7,8].

The back stress of a pile-up, which results from cumulative stress fields from each individual dislocation and therefore depends on the size of the pile-up and the number of

dislocations in it, tends to counteract the externally applied stress. This leads to a lower resultant stress state for dislocation slip [9]. Such a model has been widely used as an explanation for the empirical Hall–Petch relationship [9–11], which relates the yield strength of a polycrystalline material to its grain size by the equation $\sigma_y = \sigma_0 + kD^{-\frac{1}{2}}$, where D is the average grain diameter. The friction stress σ_0 is the stress required to sustain dislocation motion in the interior of a grain [12,13], while the $kD^{-\frac{1}{2}}$ term is the grain boundary contribution to yield strength [12]. k is often referred to as the Hall–Petch coefficient, and usually captures the average effect of the grain boundaries in the polycrystal. A recent reassessment of much of the literature data concerning grain size effects on yield strength by Dunstan and Bushby [14] has cast doubt on the Hall–Petch relationship, and attempts to rationalise it with other size effects.

The Hall–Petch coefficient has traditionally been obtained by mechanical testing of samples with varying

* Corresponding author.

E-mail addresses: yi.guo@materials.ox.ac.uk, guoyi_ernest@yahoo.com (Y. Guo).

grain diameter. Hyun et al. [15] have reported $k = 0.25 \text{ MPam}^{0.5}$ for grade 2 commercially pure titanium (CP-Ti) deformed at room temperature under tension, while Lederich et al. [16] found $k = 0.18 \text{ MPam}^{0.5}$ and $k = 0.40 \text{ MPam}^{0.5}$ for pure Ti deformed under tension at 575 and 295 K, respectively. For room-temperature compression, Salem et al. [17] reported $k = 0.67 \text{ MPam}^{0.5}$ for CP-Ti. Although $\sigma_y = \sigma_0 + kD_{GB}^{-1}$ has now been shown to support macromechanical testing data better than the Hall–Petch equation [14], the Hall–Petch coefficients available in the literature do allow the overall effects of crystal structure, alloying additions and other factors on the relative effectiveness of grain boundary strengthening to be assessed. It is to be expected that the nature and geometry of individual grain boundary types should have a pronounced effect on the intensity of local stress concentrations generated [18,19]. Amongst others, Sangid et al. [20] suggest that the slip band–grain boundary interaction is strongly affected by the character and structure of the grain boundaries. This suggests that boundaries with different characteristics should have different resistances to slip transfer. Therefore, an investigation into the strengthening mechanisms of individual grain boundaries is of theoretical and practical importance.

A large body of theoretical and modelling work has been focused on predicting the resistance to slip transfer using boundary related parameters, as has been reviewed by Morris [21]. Some of the proposed models require grain boundary parameters that cannot be measured directly, while others contain parameters that depend on pre-knowledge of k , rendering those models descriptive but not predictive. The research of Bata and Pereloma [13] suggested a relatively independent model, but this suffers from difficulties of accurately determining the grain boundary strain energy and ignores stress concentrations that might arise near the grain boundary. Theoretical work by Eshelby et al. [22], on the equilibrium spacing of dislocations, proposed a solution to modelling the stress concentration as a result of slip band–grain boundary interactions. This model, illustrated in Fig. 1, consists of an array of edge dislocations blocked by a grain boundary. This causes a stress concentration at the tip of the slip band in the neighbouring grain. This stress concentration, when resolved to the shear plane of the pile-up, attenuates in a “one over square root distance” fashion directly ahead of the pile-up away from the grain boundary. The resolved shear stress τ can thus be written as

$$\tau = \tau_0 + \frac{K}{\sqrt{r}} \quad (1)$$

where K describes the stress intensity of the stress field and r is the distance from the grain boundary.

Britton et al. [23] recently mapped the stress distribution near the head of a blocked slip band using the high-resolution electron backscatter diffraction (HR-EBSD) technique [24,25] and found the stresses to be consistent with the Eshelby–Frank–Nabarro model. The stress intensity factor

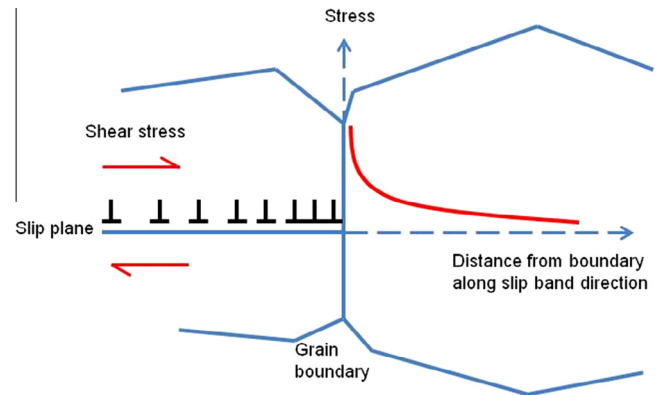


Fig. 1. Eshelby's model of dislocation pile-up at a grain boundary. The red curve to the right of the grain boundary represents the stress distribution ahead of the blocked slip band. (For interpretation of the references to colour in this figure legend, the reader is referred to the web version of this article.)

K can be obtained by curve fitting the resolved shear stress line profile ahead of the pile-up. This study provided a method to directly measure the stress intensity factor associated with an individually selected slip band–grain boundary interaction. It is therefore important to extend such measurement to different slip band–grain boundary interactions for the systematic evaluation of the strength of the grain boundary in terms of the alignment between crystal slip systems.

The stress concentration accumulated by the dislocation pile-up can be redistributed along the grain boundary if the Burger's vector of a grain boundary dislocation dissociated from the matrix dislocation is within the boundary plane in which it can then glide. This grain boundary gliding mechanism was described in Refs. [26,27]. If the grain boundary dislocations have a component out of the grain boundary plane, ledges can be created, which can lead in turn to the nucleation of boundary cracks [28]. This has been observed by Lee et al. [29] via an in situ transmission electron microscopy study. The most common stress relief mechanism is the generation of new dislocations in the neighbouring grain [30–36].

This could be done by several experimentally observed mechanisms:

- (1) direct transfer, when the incoming slip plane shares a common intersection with the outgoing slip plane on the grain boundary, and the Burger's vectors of the two slip systems are equal, i.e. this transfer mechanism leaves no residual Burger's vector at the grain boundary and is akin to cross-slip for screw dislocations;
- (2) transfer with residual grain boundary dislocation. This mechanism is accomplished by dislocation absorption and subsequent re-emission. The emitted dislocations could either connect to the previous slip band or be displaced along the grain boundary [34]. An energy barrier proportional to the magnitude of

the residual Burger's vector has been proposed to play a crucial role in this type of transfer mechanism [20,36]; and

- (3) new dislocation sources could be activated due to local stress concentration generated around the tip of a blocked slip band. For this type of dislocation to glide across the whole grain, the resolved shear stress on the slip plane must be sufficiently large, otherwise they cease propagating after a short distance from the grain boundary and other, more mechanically favourable, dislocation sources could be activated [10,11,36].

Early research by Livingston and Chalmers [33] attempted to predict which slip system is more favourable during a slip transfer process, and for this purpose the following formula was proposed:

$$N_{ij} = [(e_i \cdot e_j)(g_i \cdot g_j) + (e_i \cdot g_j)(e_j \cdot g_i)] \quad (2)$$

where e is the slip plane normal and g is the slip direction. The subscripts i and j represent two slip systems, one on either side of a grain boundary. Slip transfer is expected to activate the slip system in the neighbouring grain that maximises N_{ij} , with easier slip transfer indicated by a higher value of the maximum N_{ij} . This criterion emphasises the importance of geometric alignment on the choice of transferred slip system. Later work by Shen et al. [31] pointed out the importance of incorporating a resolved shear stress on slip transfer and a new model was proposed:

$$N'_{ij} = (L_i \cdot L_j)(g_i \cdot g_j) \quad (3)$$

where L is the lines of intersection between grain boundary plane and the planes of incoming (subscript i) and outgoing (subscript j) slip systems. A schematic showing the geometry of the slip plane alignment can be seen in Fig. 2.

Slip transfer is again favoured for slip systems with the highest N'_{ij} , i.e. the angles between L_i , L_j and g_j , g_i should be minimized. The transferred slip plane is therefore the one that maximises N'_{ij} and the slip direction is the one that has the highest resolved shear stress. While this model was successful in predicting all four boundary/pile-up configurations studied by Shen et al. exceptions were found by Lee et al. [35], who showed that, in some cases, systems that generate large grain boundary dislocations cease to operate even when the resolved shear stress is highest. Taking into account this issue, the slip transfer criteria suggested by Lee, Robertson and Birnbaum (LRB criteria) consists of three aspects:

- (1) the geometric alignment factor N'_{ij} as shown in Eq. (3) should be maximised;
- (2) the magnitude of the residual Burgers vector as the difference between incoming and outgoing dislocations should be minimized; and

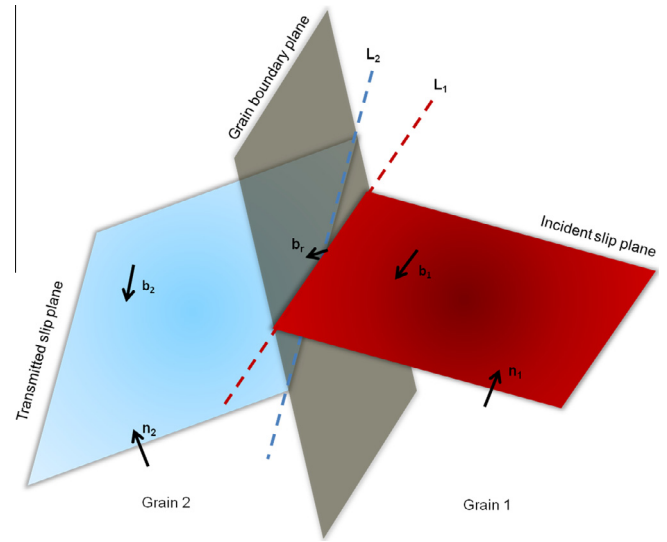


Fig. 2. Schematic showing the geometric configurations between two slip systems intersecting a grain boundary. L is the line of intersection between the slip plane and grain boundary, n is plane normal, and the Burgers vector \mathbf{b} is used to represent the slip direction g .

- (3) the resolved shear stress on the outgoing slip system imposed by the incoming slip system should be maximised.

Although derived from a study of face-centred cubic metals, the LRB criteria have had some success in studying the slip transfer process in hexagonal close-packed titanium alloys [37].

The first and second points in LRB can be combined if the Burgers vector, \mathbf{b} , is used to describe the slip direction, g , in Eq. (3). In reality, Eq. (3) is difficult to apply because in the current experimental conditions it is not easy to determine L .

As an alternative, Werner and Prantl [38] suggested that the slip plane normal n could be used to replace L , as the angle between the slip plane normal could never exceed the angle between the intersection lines with the grain boundary irrespective of the grain boundary orientation. Therefore an alternative equation that takes account of both the geometric alignment and the residual Burgers vector can be written as:

$$M = \frac{(n_i \cdot n_j)(\mathbf{b}_i \cdot \mathbf{b}_j)}{|\mathbf{b}_i||\mathbf{b}_j|} \quad (4)$$

where n and \mathbf{b} are the slip plane normal and the Burgers vector, respectively.

In this research, the factor M in Eq. (4) will be employed to investigate local slip system alignments and the correlation between M and the stress intensity factor for a collection of slip band–grain boundary pairs will be analysed. Furthermore, a comparison of the M factors will be made between grain boundaries with and without the occurrence of obvious slip transfer. The results are interpreted together with the resolved shear stress of various slip systems.

Table 1
Chemical composition of the as-received grade 1 CP-Ti [23].

Element	Fe	O ₂	N ₂	C	Ti
Composition	0.35 wt.%	700 ppm	35 ppm	0.01 wt.%	Balance

2. Materials and experimental procedures

The material used in this research was commercial purity titanium supplied by Timet UK Ltd. The chemical composition is listed in Table 1 [23]. Tensile test pieces with gauge dimensions of 30 mm × 3 mm × 1 mm were cut using electron discharge machining. The long axis of the tensile piece was along the rolling direction of the as-received bar. The tensile pieces were heat treated in a vacuum at 830 °C for 24 h to grow the grain size to an average of ~300 μm. Samples were then ground using silicon carbide paper down to 4000 grit followed by chemical–mechanical polishing using a 50 nm colloidal silica suspension. The colloidal silica polishing was followed by etching using a solution with 1% HF and 10% HNO₃ in water to remove the oxide and hydride layers, which severely degrade the quality of electron backscattered patterns. This polish–etch–polish process was repeated until a crisp grain boundary structure was visible under an optical microscope with polarised illumination.

The sample was deformed under tension to 1% plastic strain measured by in situ digital image correlation. The applied stress reached a maximum value of 235 MPa. Optical microscopy and scanning electron microscopy (SEM) imaging were used to identify various slip band–grain boundary interactions. EBSD maps were then acquired, including a number of boundaries with blocked slip bands and a number of boundaries with transferred slip bands using a JOEL JSM 6500 scanning electron microscope. The maps had an average size of 10 μm × 25 μm and were obtained at 20 kV with a 14 nA beam current over a square array of 0.2 μm step size. At each interrogation point the EBSD pattern, consisting of 1000 × 1000 pixels, was captured and saved in TIFF image format with 12-bit depth using OIM Data Collection V5.

For cross-correlation, the patterns were transformed into the Fourier domain and filtered to remove high-frequency noise and low-frequency background gradients. For each grain, a reference point was picked towards the interior of the grain, where it was assumed that the stress state was relatively low and uniform. For each EBSD pattern, 50 regions of interest (ROIs), 256 × 256 pixels in size, were selected, with one ROI at the middle of the pattern, 19 others surrounding it in a ring and the remaining 30 randomly distributed across the pattern. These ROIs on test patterns were compared with the corresponding parts on the reference pattern using cross-correlation [39], with which pattern shifts as small as 0.02 pixels can be detected [40]. These pattern shifts were used to fully determine the displacement gradient tensor (DGT) using the assumption that the stress perpendicular to the sample surface is zero [41]. Locally the lattice rotations can be quite large, so

the pattern remapping algorithm developed by Britton and Wilkinson [25] was used. This involves using a first pass of cross-correlation analysis to estimate a finite lattice rotation, which is used to remap the test pattern intensities in a virtual reorientation of the test region. A second pass of cross-correlation analysis is then used to determine the lattice strains and a correction to the lattice rotation. The DGT from the first and second passes are combined to give a total deformation gradient F , from which the Green strain tensor (E) was obtained: $E = \frac{1}{2}(F^T F - I)$. These elastic strain fields were then used to calculate stress fields using elastic constants (in GPa) for titanium: $C_{11} = 162.4$ $C_{33} = 180.7$ $C_{44} = 117$ $C_{66} = 35.2$ $C_{13} = 69.0$ [42]. The polar decomposition of F into the product of rotation and stretch tensors using singular value decomposition methods enables the lattice rotation to be determined. These finite rotation tensor were used to estimate six infinitesimal rotation gradients using procedures documented in Ref. [23] and linked to six out of the nine components of Nye's dislocation tensor [43]. The remaining three components are associated with lattice rotation gradients along the depth of the sample and therefore can only be determined using a 3-D profiling technique.

For geometrically necessary dislocation (GND) calculations of α -Ti, the following dislocation types were used: three $\langle a \rangle$ screws and six $\langle c + a \rangle$ screws; three $\langle a \rangle$ edges on the basal plane; three $\langle a \rangle$ edges on the first-order prismatic plane; six $\langle a \rangle$ edges on the first-order pyramidal plane; and 12 $\langle c + a \rangle$ edges on the first-order pyramidal plane [44]. The GND density for each type of dislocation is found using a standard linear programming algorithm by minimizing the possible total GND line energy [45]. The need for energy minimization mean that the GND density presented in this paper is a lower-bound estimation (fuller details in [45]).

It is important to note that the absolute strain state of the reference pattern is not known. Therefore the elastic strains presented here are relative values. However, this uncertainty does not affect the GND density as it is only related to lattice curvatures [46].

The HR-EBSD code initially reports stresses in the external sample reference frame. For slip band–grain boundary interactions that lead to stress concentration, these stresses were rotated such that the shear stress on the slip plane of the deforming grain in the Burgers vector direction was obtained across the two grains. From the rotated resolved shear stress field, line profiles were extracted along the direction of the pile-up. The stress intensity factor K was then determined by fitting the stress line profile using a non-linear method to the equation proposed in Ref. [23]:

$$\sigma_{31}^r = A + K/\sqrt{X + B} \quad (5)$$

where σ_{31}^r is the resolved shear stress imposed by the dislocation pile-up in the neighbouring grain and X is the distance along the line profile away from grain boundary. The constant A is introduced to allow for uncertainty of the

stress state at the reference point, while the constant B is introduced to allow for the uncertainty of the grain boundary position.

For a number of the blocked slip bands, atomic force microscopy (AFM) was used to determine the height of the slip bands. A Pacific Nanotechnology Nano-R with SPM Cockpit model atomic force microscope was used in contact mode to map the surface topography over regions $45\ \mu\text{m} \times 45\ \mu\text{m}$. Images were analysed online and topography changes across the slip band were averaged over several points along the slip band.

3. Results

Analysing the HR EBSD data from many slip band–grain boundary intersections allow us to identify three broad categories of slip band–grain boundary interactions: (1) a blocked slip band with a stress concentration ahead of it; (2) slip transfer, where the slip band in one grain continues into a connected slip band in the neighbouring grain; and (3) a blocked slip band with no long-range slip band in the neighbouring grain but no obvious stress concentration. We give the results for each of these categories in the next three sections.

3.1. Blocked slip band that lead to stress concentration

This type of interaction features a blocked slip band in one grain with no macroscopic slip transfer into the neighbouring grain, observed from surface topography, but localised stress concentration around the intersection point between the slip band and the grain boundary observed with HR-EBSD.

One example of such interactions is shown in Fig. 3. The slip band was formed to accommodate macroscopic tensile loading (for all images in this paper the tensile direction is horizontal with respect to the image), as revealed on the EBSD image quality map (Fig. 3a). No slip transfer or slip band formation was observed in the neighbouring grain. The orientation relationship between the two grains is close to a 70° rotation about the x_1 axis, as revealed by the superimposed unit cell structures (the Euler angles for all the grain pairs reported in this research can be found in the supplementary material). The slip plane of the slip band was found by trace analysis and the crystal orientation from EBSD and is indicated in red. This slip system corresponds to a low critical resolved shear stress (CRSS) $\langle a \rangle$ prismatic slip system that has a high (0.50) Schmid factor. The HR EBSD output of the full stress tensor is illustrated in Fig. 3b. The stress concentration induced by the blocked slip band is revealed most clearly in the σ_{11} and σ_{12} components. The stress tensor shown in Fig. 3b is measured in a sample frame as defined by x_1 and x_2 (the x_3 component is perpendicular to the image surface and pointing into the page). Fig. 3c shows a more useful axis system, x_1^r x_2^r x_3^r , which is described by the direction of the Burgers vector (x_1^r) and the direction perpendicular to it (x_2^r) of the active

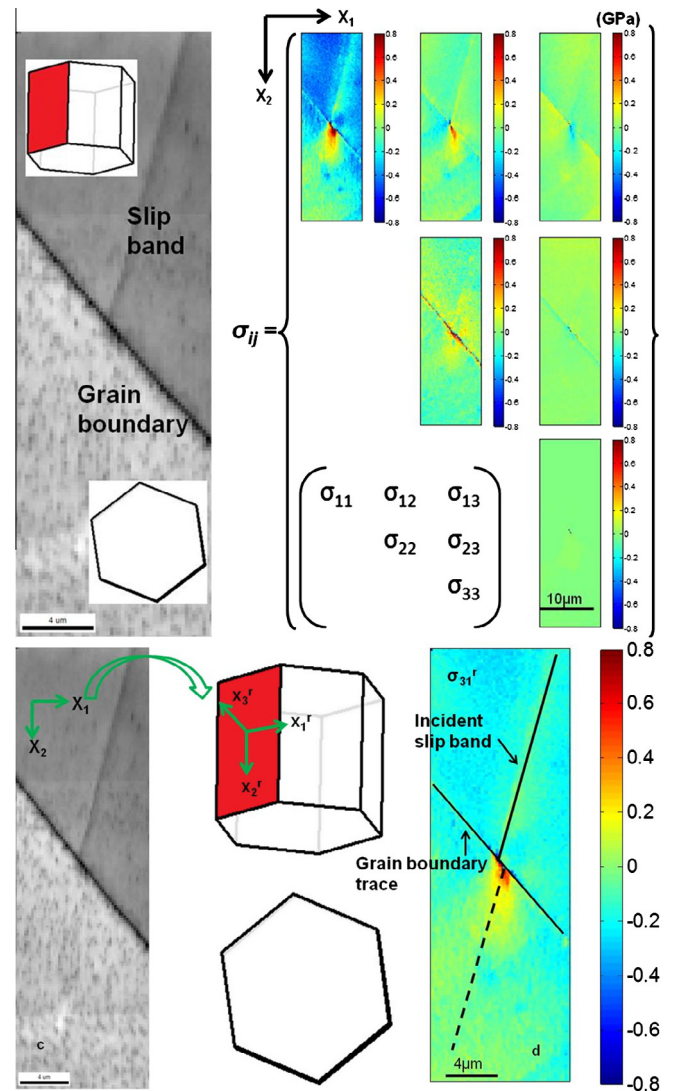


Fig. 3. (a) EBSD image quality map of a blocked slip band with grain orientation overlaid; (b) HR EBSD stress output; (c) coordinate system defined on the sample reference frame (x_1 x_2) and the slip plane reference frame (x_1^r x_2^r x_3^r); (d) the σ_{31}^r component of the stress tensor after rotation, the dashed line representing the direction along which the stress profile is extracted (all colour scales are in GPa).

slip system of the deformed grain. The shear stresses were resolved onto the active slip system of the deforming grain across the full field of the maps covering both grains (Fig. 3d). This means that in the undeformed grain the stress is not aligned with any particular slip system of that grain, but instead uses the appropriate plane and direction to best show the large shear stresses generated ahead of the blocked slip band.

A line scan along the direction of the slip band on the upper grain but extended into the lower grain (indicated by the dashed line) was extracted and the resulting stress profile is shown in Fig. 4. These data points fit well with the model proposed by Eshelby et al. [22].

Fitting the experimental stress profile with Eq. (5) allows a K value of $0.78 \pm 0.08\ \text{MPa m}^{1/2}$ to be obtained for this

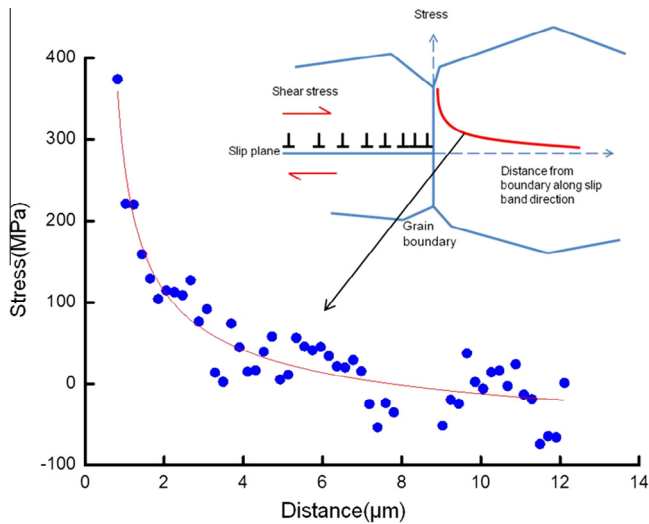


Fig. 4. Stress concentration ahead of the blocked slip band, as in Fig. 3d, with comparison to the model described by Eshelby et al. [22].

boundary, where the error indicates the standard error from the best-fit parameters. The same procedure was performed for four other boundaries in this category.

The results are summarized in Fig. 5, which shows the resolved shear stress maps overlaid with corresponding grain orientations, indicating different grain boundary geometries, along with the stress variation on a line directly ahead of the slip line. The K value, as obtained from fitting each stress profile with Eq. (5), is indicated for each grain boundary, and the values of the constants A and B are included in Supplementary Table 1. The LRB criterion

was employed in such a way that the combination of the M factor (Eq. (3)), between the incoming slip system and various of possible slip systems in the neighbouring grain, and the resolved shear stress (RSS), described by the Schmid factor (S), were used to characterise each case of interaction. For all five slip band–grain boundary interactions in Figs. 3 and 5, trace analysis revealed that each of the slip bands were due to $\langle a \rangle$ prismatic slip. The best alignment (i.e. the highest M) between these prismatic slip systems with possible $\langle a \rangle$ basal, $\langle a \rangle$ prismatic, $\langle a \rangle$ pyramidal and $\langle c + a \rangle$ pyramidal slip systems and related Schmid factors (S) are compiled in Table 2.

For this category of slip band–grain boundary interactions, the incoming prismatic slip systems are better aligned (i.e. higher M) with a $\langle c + a \rangle$ pyramidal slip system in adjacent grains; however, the magnitude of the $\langle c + a \rangle$ Burgers vector is too large compared to $\langle a \rangle$ slip and transfer would require the accommodation of additional $\langle c \rangle$. This, coupled with the higher CRSS and generally low Schmid factor, means that slip is not transferred to the $\langle c + a \rangle$ slip system. On the other hand, easy slip systems (prismatic) have poor alignment (i.e. low M), with a low Schmid factor. Those easy slip systems that do have a high Schmid factor, almost at the maximum value of 0.5, were, however, found to have the worst alignments with the incoming prismatic slip systems.

The stress ahead of the blocked pile-up is likely to depend on the number of dislocations within the pile-up. The analysis of Eshelby et al. [22] indicates that the stress intensity increases as \sqrt{N} when the number of dislocations

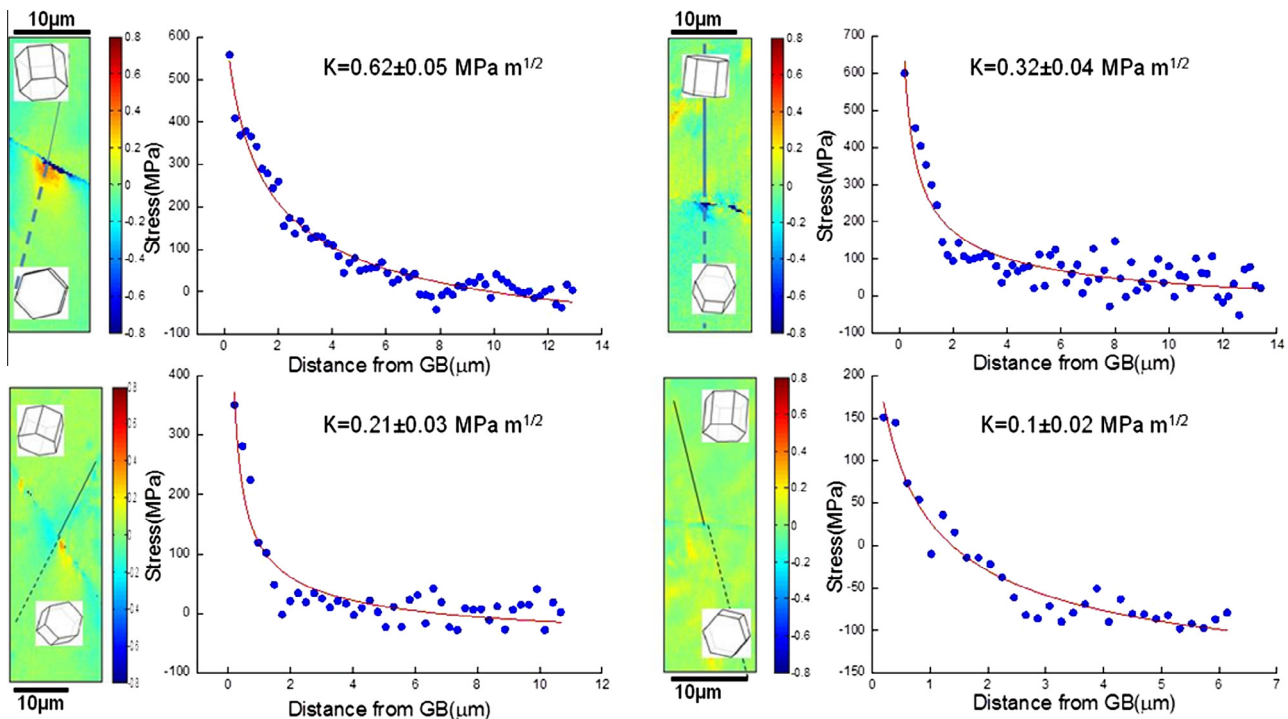


Fig. 5. Stress profile in front of the blocked slip bands and fitted stress profiles. The solid line represents the position of the incoming slip band and the dashed line is the direction along which the stress profile was extracted. The value and standard error of K obtained from fitting are shown for each stress profile.

Table 2

Geometric alignment (M) between the incoming slip plane and possible slip planes in the neighbouring grain, and the Schmidt factor on the corresponding slip system (S).

	Boundary 1 $K = 0.78$	Boundary 2 $K = 0.62$	Boundary 3 $K = 0.32$	Boundary 4 $K = 0.21$	Boundary 5 $K = 0.1$
Prismatic \rightarrow prismatic	$M_1 = 0.33$ $S_1 = 0.23$ $M_2 = 0.11$ $S_2 = 0.47$	$M_1 = 0.40$ $S_1 = 0.49$ $M_2 = 0.40$ $S_2 = 0.49$	$M_1 = 0.47$ $S_1 = 0.40$ $M_2 = 0.06$ $S_2 = 0.46$	$M_1 = 0.53$ $S_1 = 0.30$ $M_2 = 0.01$ $S_2 = 0.49$	$M_1 = 0.54$ $S_1 = 0.28$ $M_2 = 0.01$ $S_2 = 0.50$
Prismatic \rightarrow basal	$M = 0.35$ $S = 0.23$	$M = 0.48$ $S = 0.01$	$M = 0.23$ $S = 0.03$	$M = 0.28$ $S = 0.14$	$M = 0.33$ $S = 0.01$
Prismatic \rightarrow $\langle\alpha\rangle$ pyramidal	$M = 0.48$ $S = 0.02$	$M = 0.6$ $S = 0.33$	$M = 0.49$ $S = 0.25$	$M = 0.56$ $S = 0.17$	$M = 0.61$ $S = 0.20$
Prismatic \rightarrow $\langle c + a \rangle$ pyramidal	$M = 0.60$ $S = 0.33$	$M = 0.54$ $S = 0.40$	$M = 0.83$ $S = 0.27$	$M = 0.82$ $S = 0.27$	$M = 0.78$ $S = 0.11$

Only the best alignments (i.e. the highest M) are listed, except for the M_2 values in the second row of the prismatic \rightarrow prismatic alignment.

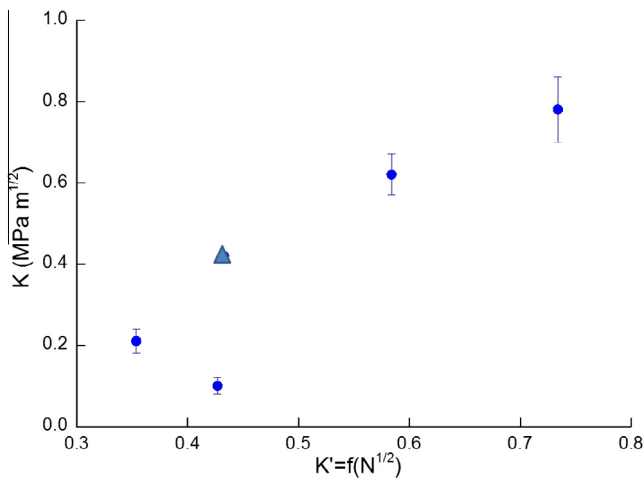


Fig. 6. K (stress intensity factor, $\text{MPa m}^{1/2}$) as a function of the square root of the number of dislocations, N , in the slip band. The horizontal axis corresponds to K' calculated from the AFM measurement of the slip band height and the vertical axis corresponds to K measured from HR-EBSD. The triangular mark is the data from the literature [23].

in the pile-up (N) is large. AFM maps, combined with the orientation of the active slip system, were used to measure the slip band heights h , from which N was obtained from knowledge of the Burgers vector length and slip direction established from EBSD. Fig. 6 shows a plot of the measured stress intensity ahead of the blocked slip band as a function of \sqrt{N} (Eq. (6)). Boundary 3 (Table 2) is not shown in Fig. 6 as the position of it on the sample surface was lost. Instead, the result obtained by Britton and Wilkinson [23] was incorporated, as indicated by the triangular mark in Fig. 6.

3.2. Slip band–grain boundary interactions that lead to slip transfer

For this type of interaction, the slip band is transferred across the grain boundary (it is not clear whether this is direct transfer or not under the resolution of the current

experimental procedure). As the ex situ experiment does not tell which slip band is the incoming band and which is the outgoing band, it is necessary to analyse two maps, one resolving the stress tensor onto the slip system for the slip band observed in the upper grain σ_{13}^U and the other resolving the slip system of the lower grain σ_{13}^L . The σ_{13}^U and σ_{13}^L variations for one of the slip band–grain boundary interactions of this category are shown in Fig. 7.

It can be seen from the stress map that there are low-level diffuse stress variations near each slip band, but no strong localised stress concentration like those seen in Fig. 3 was induced by either of the slip bands. No “one over square root distance” stress distribution can be observed ahead of either slip band. Seven instances where slip bands continued on either side of the grain boundary were mapped using HR-EBSD and in all cases there were no significant stress concentrations at the grain boundary. For the investigation of the geometric alignment, the slip band on the prismatic plane was assumed to be the incoming slip band and the M factor and the Schmidt factor S were calculated for the possible outgoing slip band. These are compared in Table 3 for the possible slip systems in the “transferred” grain.

By comparing the alignments in each column for the seven slip transfer cases, it can be seen that the observed “transferred” slip systems are the ones that have the best geometric alignment (i.e. the highest M) with the “incoming” slip system. Transferred slip bands were formed on either the prismatic slip plane or the $\langle a \rangle$ pyramidal slip plane. The transferred slip systems also tend to have a relatively high Schmid factor based on the far field applied loading. This can be noticed by comparing the S values for each column of Table 3.

3.3. Blocked slip band that does not lead to stress concentration

The third category of slip band–grain boundary interaction appears similar to the first category (Section 3.1) in

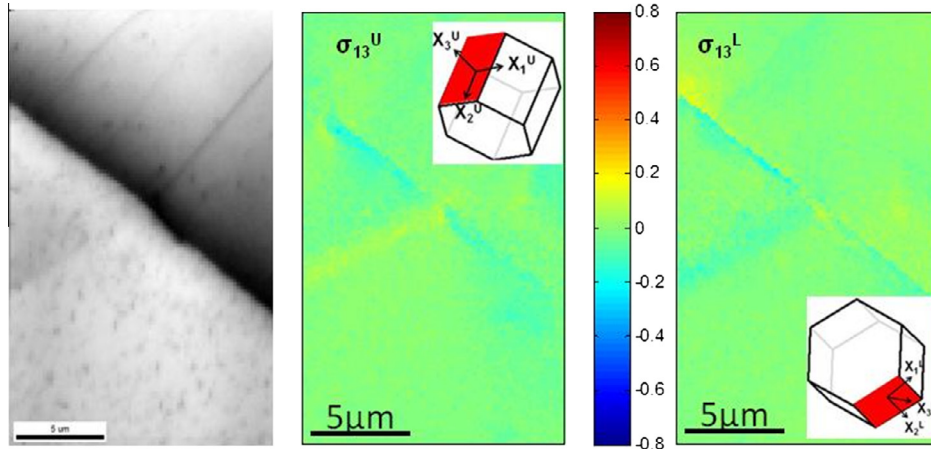


Fig. 7. SEM image showing a slip transfer feature (left) and the shear stress resolved onto the active slip system of the upper grain σ_{13}^U (middle) and the lower grain σ_{13}^L (right).

Table 3

Best alignment (maximum M) between the prismatic slip system in one grain and various slip systems in the other grain.

	Case 1	Case 2	Case 3	Case 4	Case 5	Case 6	Case 7
Prismatic \rightarrow prismatic	$M_1 = 0.94$ $S_1 = 0.26$	$M_1 = 0.46$ $S_1 = 0.33$	$M_1 = 0.95$ $S_1 = 0.33$	$M_1 = 0.41$ $S_1 = 0.39$	$M_1 = 0.84$ $S_1 = 0.47$	$M_1 = 0.73$ $S_1 = 0.43$	$M_1 = 0.91$ $S_1 = 0.47$
Prismatic \rightarrow basal	$M = 0.04$ $S = 0.03$	$M = 0.71$ $S = 0.41$	$M = 0.19$ $S = 0.03$	$M = 0.64$ $S = 0.20$	$M = 0.45$ $S = 0.18$	$M = 0.68$ $S = 0.11$	$M = 0.15$ $S = 0.05$
Prismatic \rightarrow $\langle\alpha\rangle$ pyramidal	$M = 0.67$ $S = 0.18$	$M = 0.80$ $S = 0.31$	$M = 0.78$ $S = 0.25$	$M = 0.72$ $S = 0.42$	$M = 0.9$ $S = 0.18$	$M = 0.43$ $S = 0.01$	$M = 0.50$ $S = 0.35$
Prismatic \rightarrow $\langle c + a \rangle$ pyramidal	$M = 0.56$ $S = 0.10$	$M = 0.32$ $S = 0.13$	$M = 0.52$ $S = 0.11$	$M = 0.44$ $S = 0.11$	$M = 0.66$ $S = 0.38$	$M = 0.40$ $S = 0.17$	$M = 0.76$ $S = 0.31$

Coloured cells indicate the observed slip plane of the “transferred” slip system.

that SEM imaging shows a slip band terminating at a grain boundary. The difference is that HR-EBSD reveals that these blocked slip bands do not lead to stress concentration. Two examples of the six cases mapped are shown in Fig. 8.

The distinguishing feature for this category of interaction is that no localised stress concentration can be seen around the intersection of the slip band and the grain boundary, as revealed by the σ_{13}^r resolved shear stress fields in Fig. 8. We also looked at the lower bound estimate of the GND density distributions for these cases. In one case (Fig. 8(a)) there is localised GND concentration near the head of the blocked slip band, which suggests an interaction in which some dislocation content is reflected back from the grain boundary, while in another case (Fig. 8(b)) there is no localised GND concentration but there is some evidence of increased GND density distributed along the grain boundary. The geometric alignments for the six instances of this type of interaction that were analysed are listed in Table 4.

From the comparison between the alignments with various slip systems, the blocked pile-up planes are better aligned with $\langle a \rangle$ pyramidal planes that have relatively lower

Schmid factors. Prismatic slip systems, on the other hand, generally have both lower M values and Schmid factors compared to the $\langle a \rangle$ pyramidal system. However, the M and S values of prismatic slip systems are not so distinct from those grains in Table 3 for cases where slip transfer did occur. Similar to blocked slip bands in the first category of interactions (Table 2), prismatic slip systems with higher Schmid factors have the worst alignment (M_2) with incoming slip bands.

3.4. Residual Burgers vector, stress intensity factor and M

We examined the data for correlations between the category of interaction and the residual Burgers vector between the incoming (prismatic) slip system and the various slip systems in the neighbouring grain, the stress intensity factor K , and the geometric alignment factor M . Fig. 9 plots the alignment factor M for each of the three types of slip band–grain boundary interactions, assuming transfer to either prismatic or $\langle a \rangle$ pyramidal slip systems, against the corresponding Schmidt factor S . The filled symbols in Fig. 9 represent the best-aligned $\langle a \rangle$ prism slip system, while the hollow symbols are for the best-aligned $\langle a \rangle$

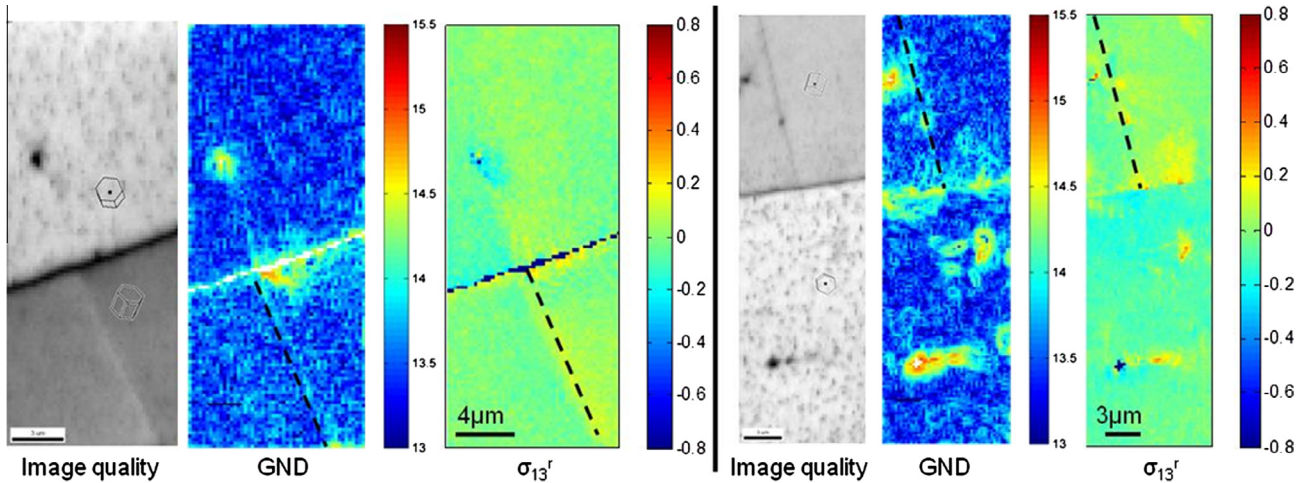


Fig. 8. Image quality map visualising a blocked slip band, the corresponding GND density map (the colour bar is on the \log_{10} scale) and the σ_{13}^r shear stress (GPa). The black dashed line indicates the slip trace. (For interpretation of the references to colour in this figure legend, the reader is referred to the web version of this article.)

Table 4

Best alignments (except for M_2 in the prismatic \rightarrow prismatic alignment) between the blocked slip plane and various slip systems in the neighbouring grain.

	Case 1	Case 2	Case 3	Case 4	Case 5	Case 6
Prismatic \rightarrow prismatic	$M_1 = 0.72$	$M_1 = 0.39$	$M_1 = 0.67$	$M_1 = 0.87$	$M_1 = 0.70$	$M_1 = 0.48$
	$S_1 = 0.35$	$S_1 = 0.34$	$S_1 = 0.44$	$S_1 = 0.27$	$S_1 = 0.48$	$S_1 = 0.38$
	$M_2 = 0.05$	$M_2 = 0.05$	$M_2 = 0.00$	$M_2 = 0.11$	$M_1 = 0.70$	$M_1 = 0.04$
	$S_2 = 0.48$	$S_2 = 0.48$	$S_2 = 0.42$	$S_2 = 0.49$	$S_1 = 0.48$	$S_1 = 0.41$
Prismatic \rightarrow basal	$M = 0.58$	$M = 0.70$	$M = 0.39$	$M = 0.39$	$M = 0.49$	$M = 0.53$
	$S = 0.04$	$S = 0.09$	$S = 0.07$	$S = 0.04$	$S = 0.13$	$S = 0.28$
Prismatic \rightarrow $\langle a \rangle$ pyramidal	$M = 0.92$	$M = 0.78$	$M = 0.74$	$M = 0.88$	$M = 0.84$	$M = 0.65$
	$S = 0.26$	$S = 0.30$	$S = 0.35$	$S = 0.21$	$S = 0.42$	$S = 0.22$
Prismatic \rightarrow $\langle c + a \rangle$ pyramidal	$M = 0.50$	$M = 0.41$	$M = 0.64$	$M = 0.60$	$M = 0.68$	$M = 0.58$
	$S = 0.11$	$S = 0.01$	$S = 0.20$	$S = 0.03$	$S = 0.14$	$S = 0.01$

Boundary 1 and Boundary 2 correspond to Fig. 8(a) and (b), respectively.

pyramidal slip systems. The background red colouring (zone 3) of the plot indicates the general tendency for the cases where slip transfer was observed to combine both good alignment (i.e. high M , i.e. $M > 0.7$) and large shear stress (i.e. high S , i.e. $S > 0.3$) on the selected slip system. Blocked slip bands, leading to a measurable stress intensity (blue background shading, zone 1), tended to be observed when the slip system alignment was relatively poor (M factor below ~ 0.5) but over the whole range of possible Schmidt factors. Blocked slip bands with very low induced stress intensity factors tend to be in a regime with an intermediate M but most often with a significant Schmidt factor. There is significant overlap between the three regions in this M – S space, possibly due to the varying amount of slip on the different slip bands observed. It seems that, although both M and S influence the situation, the alignment factor M takes priority in controlling slip transfer.

For the blocked slip bands that induced stress intensity, there was no obvious correlation between M and K . However, K tended to be smaller when the residual

Burgers vector was larger, assuming transfer to the best-aligned prismatic slip systems. The most meaningful correlation, however, was between the magnitude of K and the extent of slip in the slip band (Fig. 6).

4. Discussion

The slip band–grain boundary interactions in CP-Ti were studied with HR-EBSD, slip trace analysis and AFM. The sample was pulled to 1% strain at a low strain rate and no twinning activity was observed; therefore, the observations at this stage are useful in analysing the condition for twin nucleation and the criteria for early-stage slip transfer. Several blocked and transferred slip bands at randomly selected grain boundaries were studied and three categories of interactions could be observed.

The first category of interaction involves blocked slip bands leading to stress concentration in the neighbouring grain. Trace analysis shows that in each case the incoming slip band was due to dislocations on the prismatic slip plane

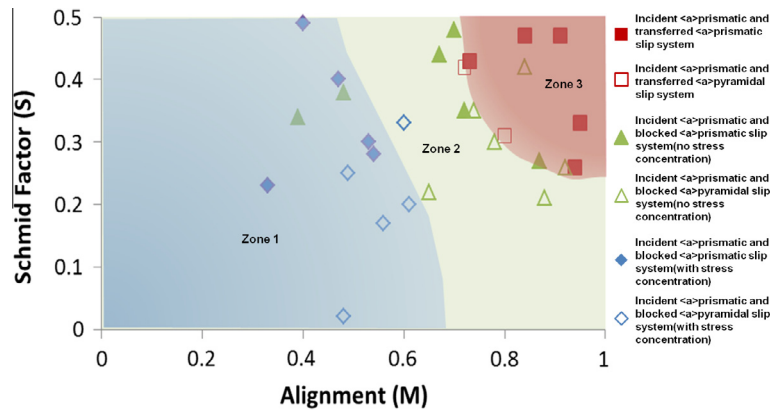


Fig. 9. Plot of the Schmid factor (S) against the M factor. The left of the plot (Zone 1) is coloured blue, which represents the zone for the first type of interaction, the middle of the plot (Zone 2) is coloured green, to represent the zone for the third type of interaction, and the top right (Zone 3) is coloured, red to represent the zone for the second type of interaction. (For interpretation of the references to colour in this figure legend, the reader is referred to the web version of this article.)

(marked red in Fig. 3), which agrees well with the macroscopic resolved shear stress analysis (i.e. Schmid factor). From the grain orientations (Figs. 3 and 5) it seems that all of the boundaries studied in this category have large rotations between the two grains, causing the basal plane normal to be close to perpendicular to each other. This generates a large misalignment of the easy slip systems. Notably, in the earlier work of Britton and Wilkinson [23], the significant misalignment of slip systems was achieved with the basal planes of the two grains close to parallel but with a rotation of $\sim 30^\circ$ about the almost shared c -axis.

For this case, the stress concentration resolved onto the pile-up plane of the incoming slip band agrees well with Eshelby's model (Fig. 4). The stress intensity factor obtained by fitting the stress profile using Eq. (4) varies from boundary to boundary in the range from 0.1 to 0.78 MPa $m^{1/2}$, with an average value of 0.41 MPa $m^{1/2}$. This average value is in agreement with the Hall–Petch coefficient of 0.40 MPa $m^{1/2}$ obtained by Lederich et al. [16] and the value of 0.40 MPa $m^{1/2}$ obtained by Armstrong et al. [47] from macroscopic tensile testing of polycrystalline Ti of varying grain size. Lederich et al. [16] also examined tensile deformation of CP-Ti at 573 K, at which elevated temperature cross-slip may facilitate slip transfer, and obtained a lower Hall–Petch coefficient of 0.18 MPa $m^{1/2}$. Salem et al. [17] obtained a higher Hall–Petch coefficient of $K = 0.67$ MPa $m^{1/2}$ from room-temperature compression testing of titanium, and ascribed the higher value to the increased population of twin boundaries, which generated large repulsive stress on incoming dislocations and therefore provided a harder barrier for slip transfer [48]. Our stress intensity values are in broad agreement with Hall–Petch coefficient obtained from tensile testing, but can be assessed in terms of the slip resistance offered by individual boundaries of varying geometry where stress intensities were measured.

When large numbers of dislocations have passed along the slip band to pile up at the grain boundary, the analysis of Eshelby et al. [22] gives the stress intensity to be

$$\sigma'_{31} \sqrt{X} = \sqrt{\frac{N\mu b\tau}{\pi(1-\nu)}} \quad (6)$$

where μ is the shear modulus, ν is Poisson's ratio and τ is the shear stress resolved onto the slip system of the slip band. Fig. 6 shows that there is a reasonable correlation between the stress intensity factors measured by HR-EBSD and \sqrt{N} estimated from AFM measurements of the slip band height. The blocked slip bands were all on the slip system for which the Schmidt factor was close to 0.5, so τ is approximately half the applied tensile stress ($\tau = 115$ MPa). In every case the stress intensity measured by HR-EBSD was of the same order of magnitude but somewhat less than the value predicted from the theory of Eshelby et al. [22] using the estimated number of dislocations in the slip band. This implies that there has been some relaxation of the expected stress intensity factor, which could be achieved by a combination of the following mechanisms: (i) some limited slip transfer with plastic flow in a small volume of material in the neighbouring grain, as seen by Britton and Wilkinson [23] and Villechaise et al. [49]; (ii) dissipation of some of the net Burgers vector by generation of grain boundary dislocations and their motion away from the head of the pile-up; or (iii) some cross-slip across the slip band to generate a pile-up of finite width [50].

Fig. 7 is an example of the slip band–grain boundary interactions which lead to slip transfer. It is not clear which slip band is the incoming one, so the stress tensor is rotated onto each pile-up plane individually. As shown in Fig. 7, there is no localised stress concentration induced by shear stress on the active slip plane, which indicates that slip transfer is a highly effective stress-relieving mechanism. For uniformity, the prismatic slip band was picked up as the incoming slip band and the other was treated as the transferred band. Therefore, the alignment factor M and Schmid factor between the “incoming” slip band and various slip systems in the neighbouring grain can be calculated. The coloured cells in Table 3 indicate the pile-up

plane of the transferred slip band. It can be seen that the transferred slip bands are on a prismatic or $\langle a \rangle$ pyramidal slip system, where the alignment is the best compared with other slip systems. For boundaries 1 and 3, the transferred slip systems are prismatic, with almost perfect alignments with the incoming slip plane, while the RSSs on those slip planes are small ($S_1 = 0.26, 0.33$, respectively). Contrary to this, the prismatic slip systems with the highest Schmidt factor ($S_2 = 0.5$) have the worst alignments with the incoming slip plane ($M_2 = 0.08$ and 0.11 , respectively). Fig. 9 shows that the M factor effectively separates different types of interactions into discrete regions. Generally speaking, slip transfer requires both high M and S (on prismatic and $\langle a \rangle$ pyramidal system), but M is the dominant factor to consider in predicting slip transfer. Although RSS plays less important role, it is important in determining how far the transferred slip band is able to propagate: a transferred slip band is likely to terminate a short distance from the grain boundary when the RSS is not large enough to sustain continuous dislocation motion. Recent work by Abuzaid et al. [51] using digital image correlation and EBSD showed that larger plastic strains accumulated in “mantle” regions near grain boundaries for which slip transfer led to small residual Burgers vectors compared to those in which slip transfer was inhibited by misalignment of the predominant slip systems to give a large residual Burgers vector.

The third type of slip band–grain boundary interaction observed in this research was blocked slip bands that lead to neither stress concentration nor slip transfer. The EBSD image quality map, GND density and σ'_{13} shear stress map for two such interactions are shown in Fig. 8. From Fig. 8a, it can be seen that a small kink is formed at the intersection point of the slip band and the grain boundary. This kink led to a localised region of GNDs being reflected back from the grain boundary into the grain containing the slip band. Neither stress concentration nor GND concentration was induced in the neighbouring grain. This is likely to be the case when the stress concentration is accommodated by localised slip close to the head of the blocked slip band. By contrast, Fig. 8b is a case where there is no localised GND concentration but more diffuse GND distribution along the grain boundary, again with no stress concentration present around the interaction point, though there seems to be a backward stress to the right of the grain boundary. Such cases are suspected to involve absorption of lattice dislocations onto the grain boundary and the motion of grain boundary dislocations away from the head of the pile-up generating local grain boundary sliding. Fig. 9 suggests that these interactions occur for intermediate values of slip system alignment. There is, however, considerable overlap between the M factors observed for cases where a clear slip transfer occurs with the two significant slip bands intersecting at the grain boundary and the M factors found for apparently blocked slip bands but where local deformation processes have successfully relaxed the local stress concentration. A full three-dimensional analysis

of the boundary geometry, along with stress and dislocation density distributions, below the sample surface might help resolve some of these issues.

5. Conclusions

The HR-EBSD technique is used to study slip band and grain boundary interactions in CP-Ti deformed under tension to 1% strain. The following conclusions can be drawn:

1. At this low strain level, slip band/grain boundary interactions can be ascribed to three types: a blocked slip band that induces stress concentration in the neighbouring grain; a blocked slip band that does not induce stress concentration in the neighbouring grain; and slip transfer.
2. Full slip transfer requires both good alignment (high M , >0.7) with the incoming easy slip system and high resolved shear stress on the outgoing slip system. For selecting the transferred slip system, local geometric alignment seems to play a more important role than the resolved shear stress.
3. In each case of slip transfer examined, HR-EBSD showed that there was no significant stress intensity associated with the intersection of the two slip bands at the grain boundary.
4. Blocked slip bands were observed when the easy slip systems in the neighbouring grain were badly aligned with the incoming slip system to give an M factor below ~ 0.7 . HR-EBSD revealed significant local stress intensity at the head of the blocked slip band in some such cases, but in many cases the stresses were not significant. The high stress intensity cases tend to have worse slip plane alignment.
5. Where significant local stresses were found, they were broadly consistent with the “one over square root of distance” variation expected from Eshelby et al.’s model [25]. The stress intensity was larger for slip bands for which AFM revealed larger plastic strains.
6. For the blocked slip bands that had no obvious stress concentrations, lattice curvature analysis indicated that GND densities were increased either in a localised feature associated with the head of the pile-up or in a more diffuse distribution along the grain boundary. These suggest that localised plastic flow was able to relieve any stresses developed by the blocked slip band.

Appendix A. Supplementary data

Supplementary data associated with this article can be found, in the online version, at <http://dx.doi.org/10.1016/j.actamat.2014.05.015>.

References

- [1] Hirth JP. Metall Trans A Phys Metall Mater Sci 1972;3:3047.
- [2] Hall EO. Yield point phenomena in metals and alloys. New York: Springer; 1970.
- [3] Wang L et al. Metall Mater Trans A 2010;41(2):421–30.
- [4] Bieler TR et al. Int J Plast 2009;25(9):1655–83.
- [5] Yoo MH, Trinkaus H. Acta Mater 1986;34:2381–90.
- [6] Zhang ZF, Wang ZG. Acta Mater 2003;51:347–64.
- [7] Dunne FPE, Rugg D. Fatigue Fract Eng Mater Struct 2008;31(11):949–58.
- [8] Sangid MD, Maier HJ, Sehitoglu H. Int J Plast 2011;27(5):801–21.
- [9] Schouwenaars R, Seefeldt M, Houtte PV. Acta Mater 2010;58:4344–53.
- [10] Hall EO. Proc Phys Soc B 1951;64:747.
- [11] Petch NJ. J Iron Steel Inst 1953;26:601.
- [12] Hansen N. Scr Mater 2004;51:801–6.
- [13] Bata V, Pereloma EV. Acta Mater 2004;52:657–65.
- [14] Dunstan DJ, Bushby AJ. Int J Plast 2013;40:152–62.
- [15] Hyun CY, Lee JH, Kim HK. Res Chem Intermed 2010;36:629–38.
- [16] Lederich RJ et al. Mater Sci Eng 1978;33.
- [17] Salem AA, Kalidindi SR, Doherty RD. Scr Mater 2002;46:419–23.
- [18] Abson DJ, Jonas JJ. Met Sci J 1970;4:24.
- [19] Li JCM. Trans TMS-AIME 1963;227:239.
- [20] Sangid MD et al. Acta Mater 2011;59:283–96.
- [21] Morris JW. In: International symposium on ultrafine grained steel, 2001.
- [22] Eshelby JD, Frank FC, Nabarro FRN. Philos Mag 1951;42:351–64.
- [23] Britton TB, Wilkinson AJ. Acta Mater 2012;60:5773–82.
- [24] Wilkinson AJ, Meaden G, Dingley DJ. Ultramicroscopy 2006;106(4):307–13.
- [25] Britton TB, Wilkinson AJ. Ultramicroscopy 2012;114:82–95.
- [26] Skrotzki W et al. Acta Metall 1988;36(4):983–94.
- [27] Forwood CT, Clarebrough LM. Philos Mag 1981;44(1):31–41.
- [28] Varin RA, Kurzydowski KJ, Tangri K. Mater Sci Eng 1987;85:115–26.
- [29] Lee TC, Robertson IM, Birnbaum HK. Acta Metall 1989;37(2):407–15.
- [30] Lim LC, Raj R. Acta Metall 1985;33(8):1577–985.
- [31] Shen Z, Wagoner RH, Clark WAT. Scr Metall 1986;20:921–6.
- [32] Lee TC, Robertson IM, Birnbaum HK. Acta Metall Mater 1992;40:2569–79.
- [33] Livingston JD, Chalmers B. Acta Metall 1957;5:322–7.
- [34] Shen Z, Wagoner RH, Clark WAT. Acta Metall 1988;36(12):3231–42.
- [35] Lee TC, Robertson IM, Birnbaum HK. Scr Metall 1989;23:799–803.
- [36] Lee TC, Robertson IM, Birnbaum HK. Philos Mag 1990;62(1):131–53.
- [37] Shirokoff J, Robertson IM, Birnbaum HK. In: Proceedings of the MRS 1993 fall meeting. Boston, MA: MRS; 1994. p. 263–272.
- [38] Werner E, Prantl W. Acta Metall Mater 1989;38(3):533–7.
- [39] Britton TB, Wilkinson AJ. Ultramicroscopy 2011;111(8):1395–404.
- [40] Wilkinson AJ, Meaden G, Dingley DJ. In: Adams BL, Schwartz AJ, Kumar A, editors. Electron backscatter diffraction in materials science. New York: Springer; 2009.
- [41] Dingley DJ et al. J Electron Microsc 2010;59(Suppl 1):155–63.
- [42] Viswanathan GB et al. Acta Mater 2005;53(19):5101–15.
- [43] Nye JF. Acta Metall 1953;1:153.
- [44] Jones IP, Hutchinson WB. Acta Metall 1981;29:951–68.
- [45] Britton TB et al. Proc R Soc A 2010;466:659–719.
- [46] Wilkinson AJ, Randman D. Philos Mag 2010;90(9):1159–77.
- [47] Armstrong R et al. Philos Mag 1962;7(73):45–58.
- [48] Yoo MH. Metall Trans A 1981;12(3):409–18.
- [49] Vilechaise P, et al. In: 12th International symposium on superalloys, 2012.
- [50] Sauzay M, Moussa MO. Int J Fract 2013;184:215–40.
- [51] Abuzaid WZ et al. J Mech Phys Solids 2012;60:1201–20.